

# Achieving Both Enhanced Voltage and Current through Fine-Tuning Molecular Backbone and Morphology Control in Organic Solar Cells

Huan-Huan Gao, Yanna Sun, Yao Cai, Xiangjian Wan,\* Lingxian Meng, Xin Ke, Shitong Li, Yamin Zhang, Ruoxi Xia, Nan Zheng, Zengqi Xie, Chenxi Li, Mingtao Zhang, Hin-Lap Yip, Yong Cao, and Yongsheng Chen\*

This work is dedicated to the 100th anniversary of Nankai University and the 100th birth anniversary of Academician Ruyu Chen

It is a great challenge to simultaneously improve the two tangled parameters, open circuit voltage ( $V_{oc}$ ) and short circuit current density ( $J_{sc}$ ) for organic solar cells (OSCs). Herein, such a challenge is addressed by a synergistic approach using fine-tuning molecular backbone and morphology control simultaneously by a simple yet effective side chain modulation on the backbone of an acceptor–donor–acceptor (A–D–A)-type acceptor. With this, two terthieno[3,2-b]thiophene (3TT) based A–D–A-type acceptors, 3TT-OCIC with backbone modulation and 3TT-CIC without such modification, are designed and synthesized. Compared with the controlled molecule 3TT-CIC, 3TT-OCIC shows power conversion efficiency (PCE) of 13.13% with improved  $V_{oc}$  of 0.69 V and  $J_{sc}$  of 27.58 mA cm<sup>-2</sup>, corresponding to PCE of 12.15% with  $V_{oc}$  of 0.65 V and  $J_{sc}$  of 27.04 mA cm<sup>-2</sup> for 3TT-CIC-based device. Furthermore, with effective near infrared absorption, 3TT-OCIC is used as the rear subcell acceptor in a tandem device and gave an excellent PCE of 15.72%.

## 1. Introduction

Recently, organic solar cells (OSCs) have enjoyed much great success mainly due to the acceptor–donor–acceptor (A–D–A) type nonfullerene acceptors (NFAs) developed in last few years,

H.-H. Gao, Y. Sun, Y. Cai, Dr. X. Wan, L. Meng, X. Ke, S. Li, Y. Zhang, C. Li, M. Zhang, Prof. Y. Chen

Key Laboratory of Functional Polymer Materials  
State Key Laboratory of Elemento-Organic Chemistry  
Centre of Nanoscale Science and Technology

College of Chemistry  
Nankai University

Tianjin 300071, China

E-mail: xjwan@nankai.edu.cn; yschen99@nankai.edu.cn

R. Xia, Dr. N. Zheng, Prof. Z. Xie, Prof. H.-L. Yip, Prof. Y. Cao

Institute of Polymer Optoelectronic Materials and Devices

State Key Laboratory of Luminescent Materials and Devices

South China University of Technology

Guangzhou 510640, China

The ORCID identification number(s) for the author(s) of this article can be found under <https://doi.org/10.1002/aenm.201901024>.

DOI: 10.1002/aenm.201901024

partially because of their characteristics such as easily tuned absorptions and energy levels, facile synthesis and purification, etc.<sup>[1–3]</sup> Thus, over 15% for single junction devices<sup>[4–7]</sup> and 17% for tandem devices<sup>[8]</sup> have been achieved. Based on theoretical prediction, it is highly possible to achieve 18% for single junction cell and 20% for tandem cells.<sup>[8]</sup> To achieve such goals, both the  $V_{oc}$  and  $J_{sc}$  need to be improved in addition to achieving high fill factor (FF). Based on the state of the art works, almost all high-performance OSC utilized a medium bandgap donor with a narrow bandgap acceptor (often a NFA), and absorb the sunlight only to  $\approx 900$  nm.<sup>[9–14]</sup> This means a large portion of sunlight ( $\approx 40\%$ ) has been wasted completely.

Thus, it is clear that optimized materials with absorption above 900 nm need to be designed. Intrinsically, these materials would have a lower lowest unoccupied molecular orbital (LUMO), which thus would generate a lower  $V_{oc}$ .<sup>[15–17]</sup> Indeed, some great effect has been dedicated to improve the performance in individually improving  $J_{sc}$  or  $V_{oc}$  but with sacrificing the other parameter. For example, extending the length of conjugation systems (6TIC,<sup>[18]</sup> 2,2'-(2Z,2'Z)-(5,10-dihexylnaphtho[1,2'b:5,6-b']di(4,4-bis(4-hexylphenyl)-4H-cyclopenta[2,1-b:3,4-b']dithiophene-2,7-diyl)bis(5,6-difluoro-3-(dicyanomethylene)-2-methyleneindan-1-one),<sup>[19]</sup> IDCIC,<sup>[14]</sup> FNIC2,<sup>[20]</sup> NCBDT,<sup>[21]</sup> etc.) or introducing electron withdrawing end group ((4,4,10,10-tetrakis(4-hexylphenyl)-5,11-(2-ethylhexyloxy)-4,10-dihydrodithienyl[1,2-b:4,5b']benzodi-thiophene-2,8-diyl)bis(2-(3-oxo-2,3-dihydroinden-5,6-dichloro-1-ylidene)malononitrile),<sup>[22]</sup> 6TIC-4F,<sup>[23]</sup> etc.) has been applied to enhance the  $J_{sc}$ , mainly by increasing the sunlight absorption. Similarly, side chain conjunction optimization (ITIC2)<sup>[24]</sup> or end group modulation (IT-M, IT-DM,<sup>[11]</sup> (3,9-bis(4-(1,1-dicyanomethylene)-3-methylene-2-oxo-cyclopenta[b]thiophen)-5,5,11,11-tetrakis(4-hexylphenyl)-dithieno[2,3-d':2,3-d']-s-indaceno[1,2-b:5,6-b']-dithiophene),<sup>[25]</sup> F-M,<sup>[26]</sup> etc.) has been explored to enhance the  $V_{oc}$  individually.

To achieve higher performance devices, it would be ideal to have both  $V_{oc}$  and  $J_{sc}$  improved all together. However, rather limited works have been reported on the simultaneously improvement of  $V_{oc}$  and  $J_{sc}$ .<sup>[14,24,27]</sup> In addition, currently most of the A–D–A NFAs designs focus on the modulation of end groups<sup>[23,28,29]</sup> and conjugated backbones<sup>[30–32]</sup> in terms of electron pulling or pushing abilities and conjugation lengths. Very rare works have been carried out on the side chain modulation with the same backbone and end structures, though it is believed that such modulation would impact both the molecular orbital energy level and the packing at solid state.<sup>[10]</sup>

With these thoughts, in this work, we reported a synergistic approach for modulating both molecular energy levels and active layer morphology by a simple introduction of alkyl chains on the backbone of an A–D–A type acceptor structure, which offers simultaneously both an enhanced  $V_{oc}$  by up-shifted unoccupied molecular orbital (LUMO) and improved  $J_{sc}$  by red-shifted absorption due to an optimized active layer. With this, two A–D–A type acceptors with near-infrared (NIR) absorption, 3TT-OCIC with the backbone modulation and 3TT-CIC without such modification (Figure 1A), have been designed and synthesized. Compared with the controlled molecule 3TT-CIC, 3TT-OCIC exhibits up-shifted LUMO and also red-shifted absorption in its blending film, which renders this molecule offer an improved  $V_{oc}$  of 0.69 V and  $J_{sc}$  of 27.58 mA cm<sup>-2</sup>, and thus enhanced PCE of 13.13% in a single junction device, corresponding to the  $V_{oc}$  of 0.65 V,  $J_{sc}$  of 27.04 and PCE of 12.15% for the control 3TT-CIC-based device. Both the different configuration distribution/energy in molecular level of these two molecules and their different behavior at solid state are believed to play a major role for their photovoltaic performance difference, supported by both experimental and theoretical studies. Furthermore, with its wide and effective absorption in the NIR range, 3TT-OCIC has also been studied as the rear subcell acceptor material in tandem device, which gave an excellent PCE of 15.72%.

## 2. Results and Discussion

### 2.1. Synthesis and Characterization

According to theoretical calculations and previous works,<sup>[8,22]</sup> high-efficiency OSC should have absorption covering visible to near infrared (NIR) absorption. Fused thieno[3,2-b]thiophene-based A–D–A acceptors have been reported by our<sup>[33]</sup> and other groups,<sup>[16,18,31]</sup> which have wide NIR absorptions and demonstrate great potentials owing to its rigid structure, long, and effective conjugation. Herein, using such a fused thieno[3,2-b]thiophene as the central unit, two NIR acceptors, 3TT-OCIC with a simple backbone modulation and 3TT-CIC without such modification, have been designed and synthesized. Furthermore, such modulation on both molecular energy levels and active layer morphology through the simple introduction of alkyl chains on the backbone could achieve enhanced  $V_{oc}$  and  $J_{sc}$  simultaneously.

The two molecules were synthesized in the conventional procedure and the detailed routes are shown in the Supporting Information (Schemes S1 and S2, Supporting Information). They were fully characterized by <sup>1</sup>H NMR, <sup>13</sup>C NMR, and mass spectrometry. The thermogravimetric analysis (TGA, Figure S1,

Supporting Information) indicates that 3TT-CIC and 3TT-OCIC exhibit high thermal stability with decomposition temperatures of 353 and 346 °C, respectively.

The density functional theoretical (DFT) calculation based on the B3LYP/6-31G(d) level by Gaussian 16 was used first to evaluate the energy levels and molecular configurations. The alkyl chains were replaced with methyl to simplify the calculation process. The optimized molecular configuration was shown in Figure 1B, in which the two acceptors all exhibit planner conjugations for their backbone. With introduction of the alkyl chains on the backbone, 3TT-OCIC showed both elevated highest occupied molecular orbital (HOMO) and LUMO energy level compared with 3TT-CIC (Figure S2, Supporting Information). The energy curves versus torsion angle of the end groups for the two acceptors was calculated to investigate the conformational states of the two acceptors. As shown in Figure 1C,D, introducing alkyl chains in the backbone causes the clear energy difference between 3TT-CIC and 3TT-OCIC. The optimized configuration for 3TT-CIC shows very small energy change at 0° and 180° with low energy difference of 1.52 Kcal mol<sup>-1</sup>. But 3TT-OCIC shows three low energy conformations (0°, 150°, and 210°) with relatively larger energy difference of 5.24 Kcal mol<sup>-1</sup>, indicating that 3TT-OCIC tends to stay with much favored configuration at a zero torsion angle (complete planar geometry structure).<sup>[10,34]</sup> These conformation differences should impact the packing mode of these two molecules and thus other solid state properties, as will be discussed below.

The ultraviolet–visible (UV–vis) absorption spectra were investigated both in dilute solution and solid films and the detailed data are summarized in Table 1. 3TT-CIC and 3TT-OCIC show almost same absorptions in chloroform with absorption maximum ( $\lambda_{max}$ ) at 806 and 809 nm, respectively (Figure S3a, Supporting Information), indicating that there is no big difference of the electronic structures at the molecular level. But at pure solid state (Figure 1E), while both materials show red-shifted absorption, 3TT-CIC demonstrates more red-shifted absorption (806 to 885 nm) than that of 3TT-OCIC (809 to 860 nm). This indicates that the minor change by introducing alkyl chain on the backbone could cause a significant difference of the intermolecular interaction and the packing at solid state, consistent with the results shown in theoretical calculation shown in Figure 1D. The optical bandgaps of these two molecules deduced from the solid absorption edges are 1.23 and 1.29 eV for 3TT-CIC and 3TT-OCIC, respectively. Although 3TT-CIC shows red-shifted absorption and lower bandgap compared to that of 3TT-OCIC in pure state, the tendency is reversed in their blending film with polymer donor poly[4,8-bis(5-(2-ethylhexyl)thiophen-2-yl)-benzo[1,2-b:4,5-b']dithiophene-co-3 fluorothieno[3,4-b]thiophene-2-carboxylate] (PCE10) as will be discussed below.

The energy levels of the two molecules were measured by cyclic voltammetry measurement (Figure S3b, Supporting Information) in dichloromethane. As shown in Figure 1F, the HOMO and LUMO were estimated to be –5.24 and –3.95 eV for 3TT-CIC, respectively. After two alkyl chains were introduced, 3TT-OCIC shows an elevated HOMO (–5.22 eV) and LUMO (–3.91 eV), which is consistent with the calculation results discussed above. The elevated LUMO of 3TT-OCIC with backbone modulation by introducing alkyl chains is expected to achieve an improved  $V_{oc}$  of its corresponding device.

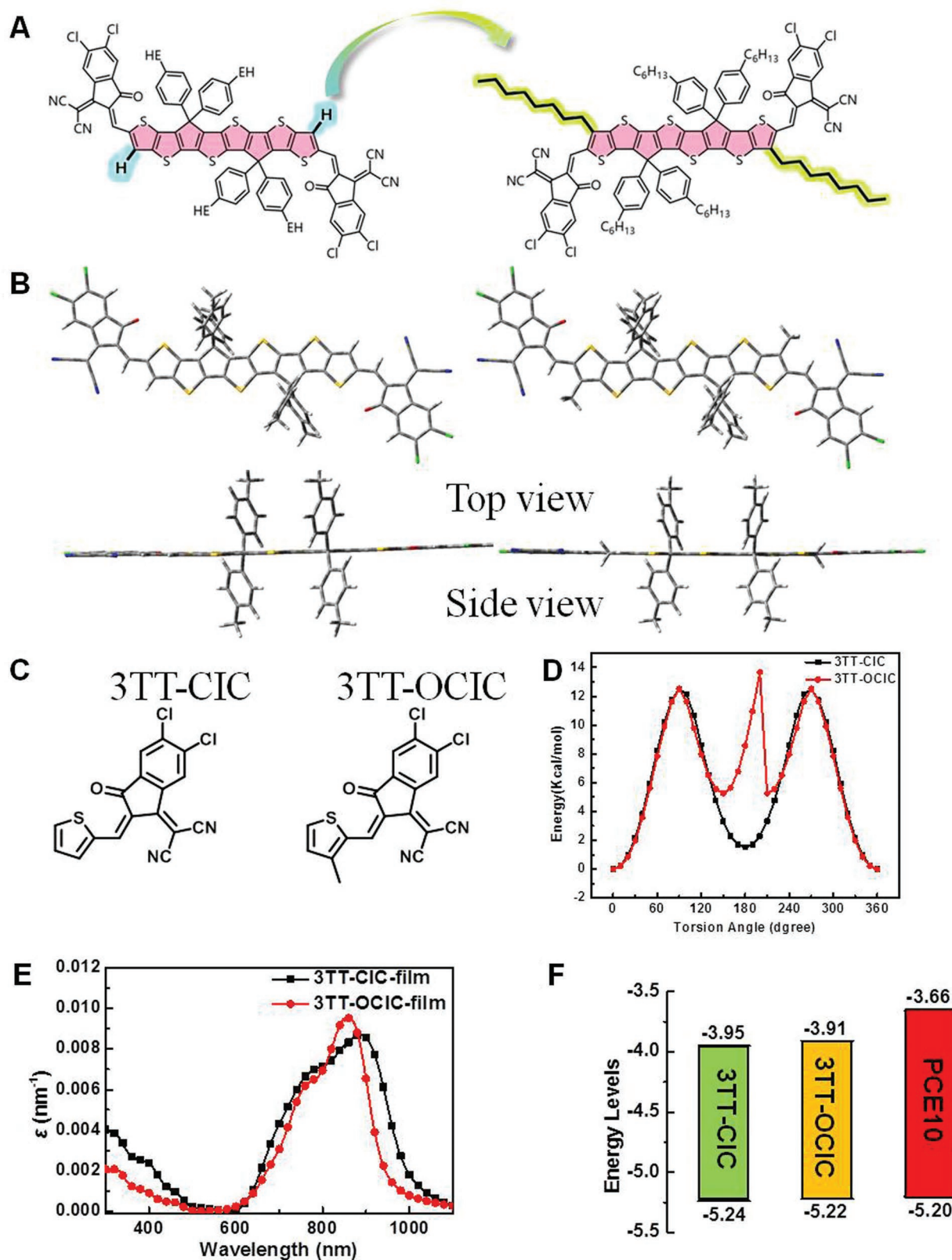


**Figure 1.** Chemical structures of 3TT-CIC and 3TT-OCIC (A), the optimized geometry conformation by DFT calculation (B), the end group rotation of 3TT-CIC and 3TT-OCIC (C) and the corresponding potential energy surface scan (D), UV-vis absorptions of 3TT-CIC and 3TT-OCIC with film thickness of 115 and 105 nm, respectively (E) and energy levels (F).

**Table 1.** The optical and electrochemical properties of 3TT-CIC and 3TT-OCIC.

Acceptors	$\lambda_{\max}^{\text{CF}}$ [nm]	$\lambda_{\max}^{\text{film}}$ [nm]	$\lambda_{\text{edge}}^{\text{film}}$ [nm]	HOMO [eV]	LUMO [eV]	$E_{\text{g}}^{\text{CV}}$ [eV]	$E_{\text{g}}^{\text{opt}}$ [eV]
3TT-CIC	806	885	1007	-5.24	-3.95	1.29	1.23
3TT-OCIC	809	860	959	-5.22	-3.91	1.31	1.29

## 2.2. Photovoltaic Performances

To evaluate the photovoltaic properties of the two molecules as acceptors, OSCs with an inverted structure (ITO/ZnO/PFN-Br/active layers/MoO<sub>x</sub>/Ag) were fabricated and optimized. The widely used PCE10 was selected as the donor polymer due to its matched energy levels and complementary absorption with the two acceptors. The devices parameters under different conditions were summarized in Tables S1–S9 in the Supporting Information, including polymer donor concentration, the weight ratio (m%) of the donor and NFA acceptors, the amount of additive (1,8-diiodine octane, DIO, vol%), thermal annealing (TA), the ratio of third component PC<sub>71</sub>BM, etc. The best performances of the two acceptor-based devices and the corresponding parameters are given in **Table 2**, and the corresponding current–voltage (*J*–*V*) curves are shown in **Figure 2A,B**. The optimized PCE10:3TT-CIC and PCE10:3TT-OCIC devices gave PCEs of 11.96% and 12.43%, respectively. The up-shifted LUMO energy level made 3TT-OCIC-based device gave an enhanced  $V_{\text{oc}}$  of 0.68 V compared with that of 3TT-CIC with  $V_{\text{oc}}$  of 0.65 V. After introducing PC<sub>71</sub>BM as the secondary acceptor, the optimized 3TT-CIC-based devices (PCE10:3TT-CIC:PC<sub>71</sub>BM) gave a PCE of 12.15% with a  $V_{\text{oc}}$  of 0.65 V and  $J_{\text{sc}}$  of 27.04 mA cm<sup>-2</sup>. But when two alkyl chains were introduced, the optimized 3TT-OCIC-based devices (PCE10:3TT-OCIC:PC<sub>71</sub>BM) exhibited a higher PCE of 13.13% with an increased  $V_{\text{oc}}$  of 0.69 V and enhanced  $J_{\text{sc}}$  of 27.58 mA cm<sup>-2</sup>.

The external quantum efficiency (EQE) curves of the optimized binary devices are shown in **Figure 2C**. The two binary devices all exhibit high EQE response from 300 to 950 nm, which is in consistent with the absorption spectra of the binary blending films, as will be discussed below. For the two optimized ternary devices, they all show efficient photo-to-electron response range from 300 to 980 nm. Meanwhile, 3TT-OCIC-based device shows widen EQE response from 880 to 1000 nm, which is consistent with its blending film absorption characteristics (**Figure 2D**).

**Table 2.** The optimized photovoltaic data of 3TT-CIC- and 3TT-OCIC-based devices under the illumination of AM 1.5G (100 mW cm<sup>-2</sup>).

Devices <sup>a)</sup>	$V_{\text{oc}}$ [V]	FF	$J_{\text{sc}}$ [mA cm <sup>-2</sup> ]	$J_{\text{sc}}^{\text{EQE}}$ [mA cm <sup>-2</sup> ]	PCE [%] <sup>b)</sup>
PCE10:3TT-CIC	0.65	0.69	26.67	24.33	11.96 (11.69 ± 0.30)
PCE10:3TT-OCIC	0.68	0.69	26.49	24.66	12.43 (12.22 ± 0.23)
PCE10:3TT-CIC:PC <sub>71</sub> BM	0.65	0.69	27.04	25.83	12.15 (11.95 ± 0.23)
PCE10:3TT-OCIC:PC <sub>71</sub> BM	0.69	0.69	27.58	26.02	13.13 (13.06 ± 0.18)

<sup>a)</sup>The device architecture is ITO/ZnO/PFN-Br/PCE10:Acceptors/MoO<sub>x</sub>/Ag. The spin-coating speed is 1200 and 1800 rpm with film thickness of 130 and 136 nm for 3TT-CIC- and 3TT-OCIC-based ternary devices, respectively; <sup>b)</sup>The PCE value was calculated from 20 devices.

As it is expected, the  $V_{\text{oc}}$  and  $J_{\text{sc}}$  of 3TT-OCIC-based ternary devices were simultaneously improved with nearly unchanged fill factors (FF) compared with that of 3TT-CIC. The enhancement of  $V_{\text{oc}}$  from 3TT-CIC to 3TT-OCIC is easy to understand as the LUMO was elevated after introducing alkyl chains on the central backbone. But the enhancement of the  $J_{\text{sc}}$  deserves more discussion, as the elevation of LUMO would generally cause less absorption and smaller  $J_{\text{sc}}$ . Note 3TT-OCIC showed blue-shifted absorption compared with 3TT-CIC in their solid film absorption (**Figure 1B**). But surprisingly, as shown in **Figure 2E**, 3TT-CIC binary film with PCE10 showed blue-shifted absorption compared with its pure film (from 885 to 867 nm). While, 3TT-OCIC blending film with PCE10 exhibited red-shifted absorption (from 860 to 885 nm). Similarly, in the ternary films with PCE10 and PC<sub>71</sub>BM, 3TT-OCIC blending film demonstrated red-shifted absorption compared with 3TT-CIC. As shown in **Figure 2F**, 3TT-OCIC ternary film showed the maximum absorption at 892 nm, compared with the maximum absorption at 860 nm for 3TT-OCIC pure film. In contrast, 3TT-CIC ternary film showed a maximum absorption at 857 nm, which was even blue-shifted compared to the 3TT-CIC pure film (885 nm). As shown in **Figure 2E,F**, there is a significant change in the absorption intensity of maximum peaks of 3TT-OCIC-based films before and after the addition of PC<sub>71</sub>BM, while there is no clear change for the 3TT-CIC-based films. This is ascribed to the change of packing behaviors of the two acceptors in their blending films after introducing PC<sub>71</sub>BM, which will be discussed below. In addition, using PC<sub>71</sub>BM as the secondary acceptor in this work, the cascade energy alignments were formed and could provide more charge transport channels and improved morphology in the ternary devices, as shown in atomic force microscopy (AFM) (**Figure 3**) and transmission electron microscopy (TEM) images (**Figure S7**, Supporting Information). Thus, based on their blend film absorption, 3TT-OCIC device should have more efficient light absorption than that for 3TT-CIC, which should generate an enhanced  $J_{\text{sc}}$  in its OSC devices. The above results demonstrate that the energy levels of 3TT-OCIC and absorption of its active layer could be effectively modulated through the simple side chain engineering on the molecular backbone, which are attributed to its observed improvement of  $V_{\text{oc}}$ ,  $J_{\text{sc}}$ , and PCE.

On the other hand, the 3TT-OCIC-based optimized device showed a good stability. As shown in **Figure S5** in the Supporting Information, it retained 97% of its initial efficiency under argon condition after 44 days. In contrast, the 3TT-CIC-based optimized device retained 86% of its initial performance under the same condition. The results demonstrate that the modulation of backbone using alkyl chains not only enhances the photovoltaic performances but also improves the devices lifetime.

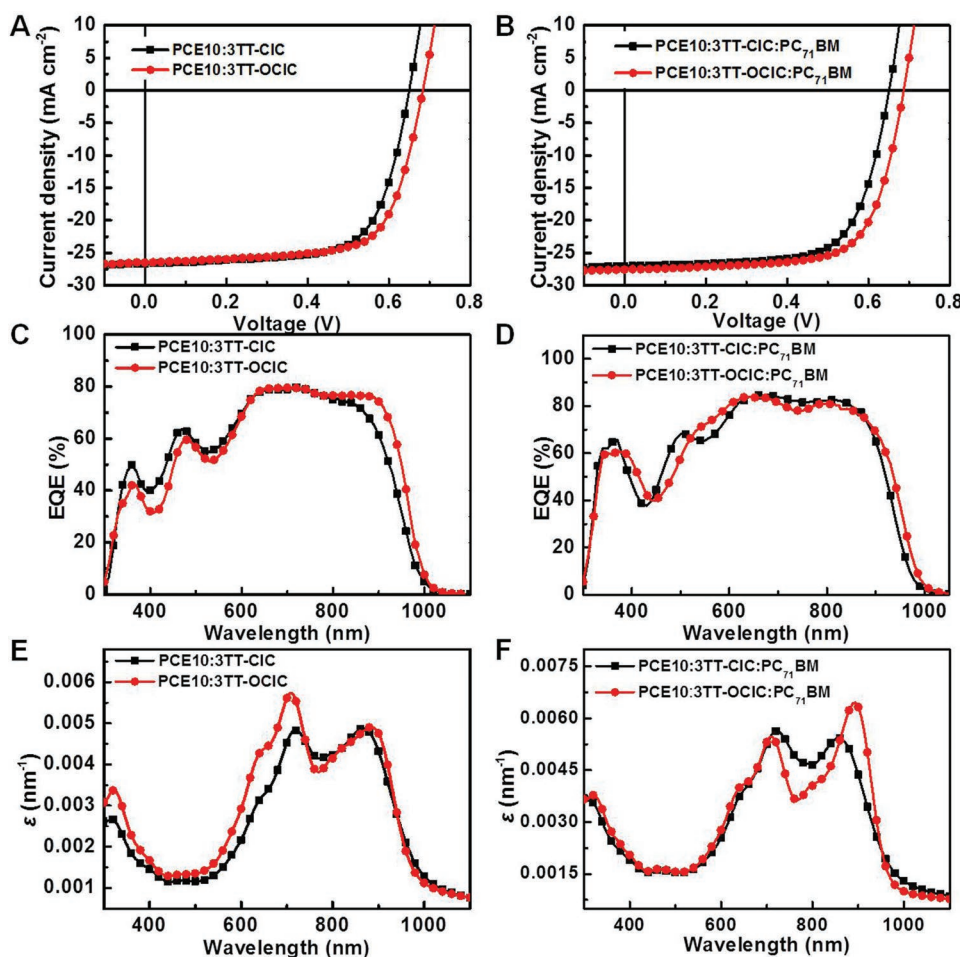


**Figure 2.** Current–voltage ( $J$ – $V$ ) (A,B) and the corresponding EQE (C,D) curves of 3TT-CIC and 3TT-OCIC–based binary and ternary solar cells, UV–vis absorption spectra with film thickness of 115 and 123 nm for the binary (E) and 105 and 120 nm for ternary blending films, respectively.

### 2.3. Morphology Study

The surprising impact of introducing alkyl chains on the backbone in the absorption and  $J_{sc}$  should be due to the different packing behaviors of the two molecules and their corresponding morphology, as their absorption in solution is almost the same. Atomic force microscopy, transmission electron microscopy, and grazing incidence wide-angle X-ray scattering (GIWAXS) were, thus, used to study the morphology of the active layers of these two molecules and compare with the morphology at pure state. As shown in Figure 3A,B, the values of root-mean-square (RMS) surface roughness of 3TT-OCIC, 3TT-CIC, and PCE10 (Figure S6, Supporting Information) are 0.841, 0.986, and 2.10 nm, respectively, which are consistent with the pristine GIWAXS results below. The 3TT-CIC– and 3TT-OCIC–based binary films exhibits similarly RMS surface roughness of 1.290 and 1.25 nm, respectively. After introducing PC<sub>71</sub>BM–, 3TT-CIC–, and 3TT-OCIC–based ternary blending films exhibit improved and suitable phase separation morphology with RMS values of 1.130 and 1.650 nm, respectively. Although there is no clear difference for these two optimized ternary films from their TEM images (Figure S7, Supporting Information), there exists significant difference from GIWAXS pattern to support

the improved  $J_{sc}$ . As shown in Figure S8 in the Supporting Information, in the pristine film, PCE10 pure film shows a clear (010) diffraction peak at  $1.64 \text{ \AA}^{-1}$ , corresponding to a  $\pi$ – $\pi$  stacking distance of  $3.86 \text{ \AA}$ . 3TT-OCIC shows a relatively weak diffraction peak with the introduction of alkyl chain in the backbone. Nevertheless, 3TT-CIC without such modification on the backbone possesses a clear (010) diffraction peak located at  $1.78 \text{ \AA}^{-1}$  in the out-of-plane (OOP) direction, corresponding to a  $\pi$ – $\pi$  stacking distance of  $3.53 \text{ \AA}$  and a possible more ordering packing. This is consistent with the pristine films absorptions of the two molecules (Figure 1E), in which 3TT-CIC exhibits red-shifted absorption compared with 3TT-OCIC.

In the binary blending films of PCE10:3TT-OCIC (Figure 3C), it shows a clear face-on diffraction peak located at  $1.71 \text{ \AA}^{-1}$  in the OOP direction, corresponding to a  $\pi$ – $\pi$  stacking distance of  $3.67 \text{ \AA}$ . In contrast, PCE10:3TT-CIC film exhibits diffraction peak at  $1.74 \text{ \AA}^{-1}$  in the OOP direction with a  $\pi$ – $\pi$  stacking distance of  $3.61 \text{ \AA}$ . The crystal coherence length (CCL) for 3TT-CIC and 3TT-OCIC in the blending films with PCE10 were estimated from Scherrer's equation ( $CCL = 2\pi k / \text{fwhm}$ )<sup>[35]</sup> by Gaussian fitting with the full-width at half-maximum (fwhm) of  $0.369$  and  $0.407 \text{ \AA}^{-1}$ , corresponding to a CCL of  $15.3$  and  $13.9 \text{ \AA}$  respectively (Table 3). Note the ternary composite films

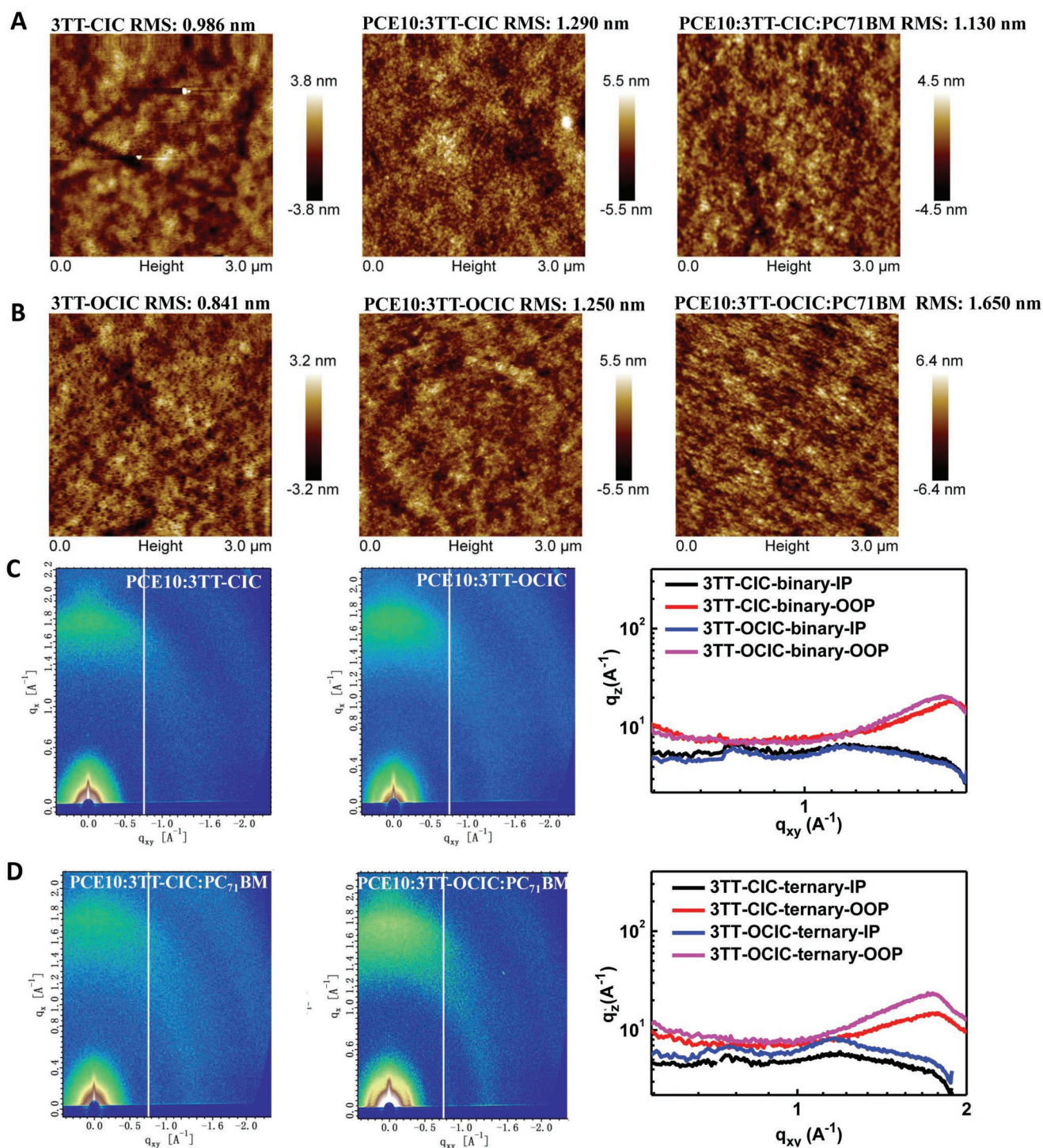


**Figure 3.** AFM images based on the pristine and the blending films based on 3TT-CIC (A) and 3TT-OCIC (B), the 2D GIWAXS patterns based on the binary and ternary blending films of 3TT-CIC (B) and 3TT-OCIC (C) and the corresponding line-cut profiles.

of the two acceptors with PCE10 and PC<sub>71</sub>BM also show the similar phenomena, i.e., a reversed trend compared with that in the two molecules pure solid state. As shown in Figure 3D, 3TT-CIC- and 3TT-OCIC-based ternary films all show clear face-on diffraction peaks in the OOP direction, in relation to a  $\pi$ - $\pi$  stacking distance of 3.71 and 3.74 Å, respectively. Moreover,

3TT-OCIC ternary film also shows a larger CCL of 13.2 nm than that of 3TT-CIC ternary film with value of 12.7 nm, indicating a better  $\pi$ - $\pi$  stacking for 3TT-OCIC at ternary film state. Thus, 3TT-OCIC blending film yields a red-shifted absorption than 3TT-CIC, which is consistent with the observed enhanced  $J_{sc}$  in 3TT-OCIC-based device. The above results demonstrate

**Table 3.** Summary of the GIWAXS parameters for the binary and ternary blending films.

Active layer	(010) $q_z^a$ [ $\text{\AA}^{-1}$ ]	fwhm <sup>b</sup> [ $\text{\AA}^{-1}$ ]	$\pi$ - $\pi$ stacking [ $\text{\AA}$ ]	CCL <sup>c</sup> [ $\text{\AA}$ ]
PCE10:3TT-CIC	1.74	0.369	3.61	15.3
PCE10:3TT-OCIC	1.71	0.407	3.67	13.9
PCE10:3TT-CIC:PC <sub>71</sub> BM	1.69	0.445	3.71	12.7
PCE10:3TT-OCIC:PC <sub>71</sub> BM	1.68	0.428	3.74	13.2

<sup>a</sup>The (010) diffraction peak in the out-of-plane (OOP) direction; <sup>b</sup>Full-width at half-maximum by Gaussian fitting; <sup>c</sup>Crystal coherence length estimated from Scherrer's equation ( $CCL = 2\pi k \text{ fwhm}^{-1}$ ).

that the minor change due to the alkyl chains on the backbone of A–D–A acceptor is critical in determining the active layer morphology. These results indicate that favorable morphology could be obtained through fine tuning molecular backbone in term of side chain engineering.

The contact angle was used to further understand the miscibility between PCE10 donor and the two acceptors (Table 4 and Figure S9, Supporting Information).<sup>[36]</sup> The surface tensions and interfacial tensions between the donor and acceptor in the blending films were obtained from their contact angle estimated following the literatures procedure (Figure S9, Supporting Information).<sup>[36,37]</sup> According to contact angle, 3TT-OCIC pure film exhibits relatively low surface tension in comparison to 3TT-CIC. Then the Flory–Huggins parameter  $\chi$  were calculated following the equation,<sup>[38,39]</sup>  $\chi \propto (\gamma_{\text{donor}}^{0.5} - \gamma_{\text{acceptor}}^{0.5})^2$  to evaluate the miscibility of the two binary blending films. The  $\chi$  parameter of PCE10:3TT-OCIC is higher than that of PCE10:3TT-CIC, demonstrating a lower miscibility and relatively higher domain purity in the new designed PCE10:3TT-OCIC device.<sup>[39]</sup> As shown in Table 4, the contact angles of PC<sub>71</sub>BM were measured under the same condition with PCE10 and the two acceptors. PC<sub>71</sub>BM showed a larger surface tension compared with PCE10 and the two acceptors, which would influence the packing behaviors of the two acceptors and their phase separation.<sup>[40,41]</sup> After introducing alkyl chains on the backbone, 3TT-OCIC-based ternary blend film demonstrated improved morphology with suitable phase separation.

#### 2.4. Charge Recombination Study

In order to fully study the excitation dissociation and charge collection properties of the two acceptor-based devices, the plots of photocurrent ( $J_{\text{ph}}$ ) versus applied voltage ( $V_{\text{eff}}$ ) were measured (Figure S10, Supporting Information). Herein,  $J_{\text{ph}} = J_{\text{L}} - J_{\text{D}}$ , where  $J_{\text{L}}$  and  $J_{\text{D}}$  are the current densities under illumination and in the dark, respectively, and  $V_{\text{eff}} = V_0 - V_a$ ,

**Table 4.** Contact angle on the surface of water and glycerol and the surface tensions of PCE10, 3TT-CIC, and 3TT-OCIC.

Films	$\theta_{\text{water}}$ [°]	$\theta_{\text{glycerol}}$ [°]	$\gamma$ [mN m <sup>-1</sup> ]
PCE10	101.81	88.45	21.44
3TT-CIC	95.87	86.35	24.63
3TT-OCIC	92.24	84.79	26.89
PC <sub>71</sub> BM	88.54	75.34	33.31

where  $V_a$  is the applied voltage and  $V_0$  is the voltage when  $J_{\text{ph}}$  is zero. As shown in Figure S10a in the Supporting Information, the devices all reach saturation ( $J_{\text{sat}}$ ) when  $V_{\text{eff}}$  reaches  $\approx 2$  V, illustrating that in higher voltage the charge recombination is minimized for the devices of both acceptor molecules. The value of  $J_{\text{ph}}/J_{\text{sat}}$  represents charge dissociation and collection probability ( $P(E, T)$ ). Under short-circuit current density and maximal power output conditions, the device based on 3TT-CIC gave a  $J_{\text{ph}}/J_{\text{sat}}$  value

of 84% and 70%, respectively. As for 3TT-OCIC, it achieved a higher  $J_{\text{ph}}/J_{\text{sat}}$  values of 91% under short-circuit current density and 87% for maximal power output condition. These indicate that the 3TT-OCIC-based device offers higher exciton dissociation and more efficient charge collection efficiency. The light-intensity dependence ( $P$ ) of  $J_{\text{sc}}$  was measured to further study the charge recombination behavior of the two devices (Figure S10b, Supporting Information). The relationship between light intensity and  $J_{\text{sc}}$  can be expressed using the power-law equation of  $J_{\text{sc}} \propto P^\alpha$ , where the component  $\alpha$  implied the extent of bimolecular recombination. The  $\alpha$  values were 0.997 and 0.999 for 3TT-CIC- and 3TT-OCIC-based devices, respectively, illustrating that the devices based on these two acceptors all showed little bimolecular recombination.

To further understand the charge recombination dynamics, the transient photovoltages were measured under a light bias with an intensity of 100 mW cm<sup>-2</sup>.<sup>[42]</sup> From Figure S11 in the Supporting Information, the carrier lifetimes were 61.9 and 77.4  $\mu\text{s}$  for 3TT-CIC- and 3TT-OCIC-based solar cells, respectively. The longer carrier lifetime indicates a weak recombination and an improved  $J_{\text{sc}}$  values for the 3TT-OCIC-based devices.

#### 2.5. Mobility

The charge mobility of the two molecules blending films were measured using space charge limit current (SCLC) method with the electron and hole only device (Figure S12, Supporting Information). The electron and hole mobility of PCE10:3TT-OCIC-based binary blend film were calculated to be  $1.36 \times 10^{-4}$  and  $1.26 \times 10^{-4}$  cm<sup>2</sup> V<sup>-1</sup> s<sup>-1</sup>, respectively, which is higher than that of PCE10:3TT-CIC blending film to be  $1.18 \times 10^{-4}$  and  $0.93 \times 10^{-4}$  cm<sup>2</sup> V<sup>-1</sup> s<sup>-1</sup>, respectively. After introducing PC<sub>71</sub>BM, the electron and hole mobility of PCE10:3TT-CIC:PC<sub>71</sub>BM blending film were enhanced to be  $1.32 \times 10^{-4}$  and  $1.24 \times 10^{-4}$  cm<sup>2</sup> V<sup>-1</sup> s<sup>-1</sup>, respectively and the electron and hole mobility of 3TT-OCIC-based blending film increases to  $1.92 \times 10^{-4}$  and  $1.83 \times 10^{-4}$  cm<sup>2</sup> V<sup>-1</sup> s<sup>-1</sup>, respectively. The mobility data is well in accordance with the blend film absorption properties.

The above results of the two molecules device dynamics analysis and mobility measurements indicate that the modulation of molecular backbone through introducing alkyl chains lead favorable effects on the device working process from the perspective of the bimolecular recombination, carrier lifetime and mobility, which is due to the induced optimal morphology change by the introduction of the side chains.

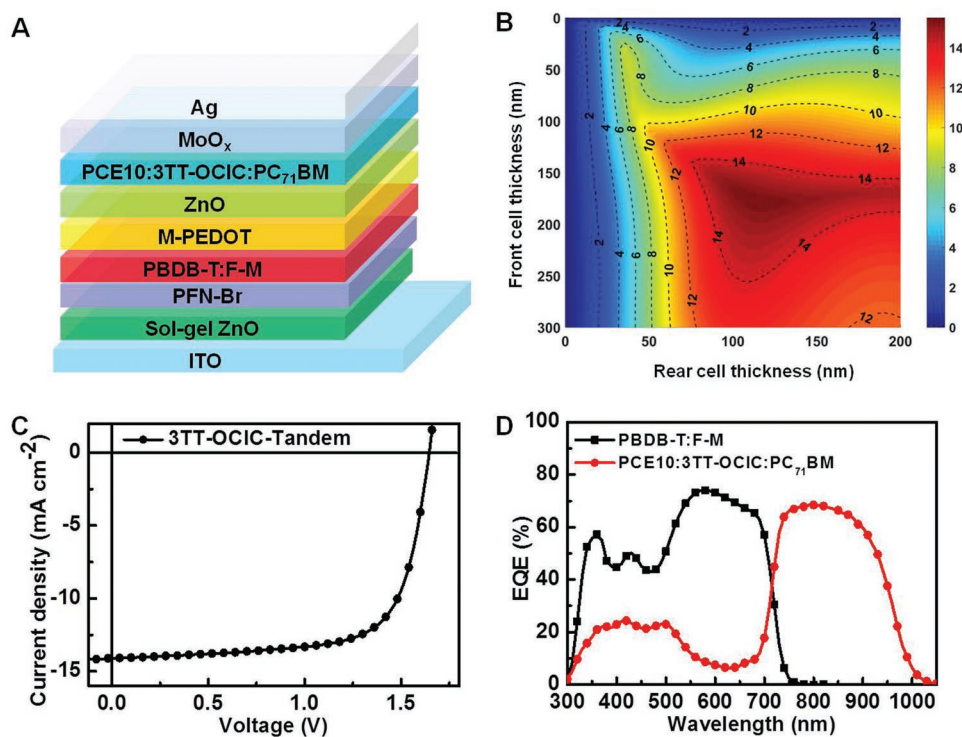


**Figure 4.** Tandem device structure (A), simulated  $J_{sc}$  as a function of thickness of the front and rear cells (B), the  $J$ - $V$  (C) and corresponding EQE (D) curves of the tandem devices.

## 2.6. Tandem Devices Fabrication

As proposed before,<sup>[43–47]</sup> high-performance tandem cells need NIR materials in rear subcells. Considering that 3TT-OCIC has NIR absorption with edge around 1000 nm, we fabricated a tandem device and used it as the acceptor in rear cell. The detailed fabrication and characterization information are shown in Supporting Information. The tandem device structure is shown in **Figure 4A**, in which PBDB-T:F-M (Figure S13, Supporting Information) was used as front cell. The optical simulation based on the transfer matrix method was conducted to provide the optimal film thickness of the subcells (Figure 4B). The simulation  $J_{sc}$  reached an optimized value of  $15.49 \text{ mA cm}^{-2}$  when the front and rear cell with the film thickness of 175 and 110 nm, respectively. The film thicknesses of the front and rear subcells were optimized and the corresponding data is shown

**Table 5.** The photovoltaic data of the tandem devices and the related subcells under one-sun irradiation (AM 1.5 G).

Device	$V_{oc}$ [V]	FF	$J_{sc}$ [ $\text{mA cm}^{-2}$ ]	PCE [%] <sup>b)</sup>
Front cell <sup>a)</sup>	0.99	0.70	15.52	10.75 (10.66 ± 0.16)
Rear cell	0.69	0.69	27.58	13.13 (13.06 ± 0.18)
Tandem cell	1.64	0.69	13.89	15.72 (15.68 ± 0.20)

<sup>a)</sup>The device architecture is ITO/ZnO/PFN-Br/PBDB-T:F-M/M-PEDOT:PSS/ZnO(NPs)/PCE10:3TT-OCIC:PC<sub>71</sub>BM/MoO<sub>x</sub>/Ag. The spin-coating speed is 1200 rpm for PBDB-T:F-M and 1800 rpm for PCE10:3TT-OCIC:PC<sub>71</sub>BM; <sup>b)</sup>The PCE values were calculated from 25 devices.

in Tables S10–S11 in the Supporting Information. With initial device optimization, a PCE of 15.72% with a  $V_{oc}$  of 1.64 V, a FF of 0.68, and a  $J_{sc}$  of  $13.89 \text{ mA cm}^{-2}$  was achieved with the front and rear cell thickness of 150 and 122 nm, respectively (**Table 5**, Figure 4C). As shown in Figure 4D, the integral  $J_{sc}$  obtained from the EQE measurements are  $13.34 \text{ mA cm}^{-2}$  for the front subcell and  $13.27 \text{ mA cm}^{-2}$  for the rear subcell, which are consistent with that measured in  $J$ - $V$  measurement under AM 1.5G illumination. The slightly lower FF and  $J_{sc}$ , compared with previous report<sup>[8]</sup> is believed due to the interconnection layer used here, which indicates further optimization is needed.

## 3. Conclusion

In summary, we reported an effective approach, i.e., synergistic modulation of molecule levels and active layer morphology through introduction of alkyl chains on the backbone of an acceptor–donor–acceptor type acceptor to improve  $V_{oc}$  and  $J_{sc}$  simultaneously. Two acceptors, 3TT-OCIC with backbone modulation and 3TT-CIC without such modification, have been designed and synthesized. 3TT-OCIC-based device gave a PCE of 13.13% with the both enhanced  $V_{oc}$  of 0.69 V and  $J_{sc}$  of  $27.58 \text{ mA cm}^{-2}$ , corresponding to the PCE of 12.15%,  $V_{oc}$  of 0.65 V,  $J_{sc}$  of  $27.04 \text{ mA cm}^{-2}$  for 3TT-CIC-based device. In addition, with its effective NIR absorption, 3TT-OCIC was used as the rear subcell acceptor material in tandem device, which gave an excellent PCE of 15.72%. These results demonstrate that  $V_{oc}$  and  $J_{sc}$  could be simultaneously improved through fine-tuning the backbone unit with a minor side chain change. Since this

approach would guarantee a well-established structure and a rather minor impact for the molecule and its solid state, it is believed this strategy could be successfully applied for a wide range of high-performance OSC molecules directly. This work would offer a new and speedy approach for designing better active materials for high-efficiency OSCs.

## Supporting Information

Supporting Information is available from the Wiley Online Library or from the author.

## Acknowledgements

The authors gratefully acknowledge the financial support from MoST (2016YFA0200200), National Natural Science Foundation of China (NSFC) (91633301, 51773095, 51873089, and 21421001), Natural Science Foundation of Tianjin City (17JCQJC44500, 17JCZDJC31100), and 111 Project (B12015).

## Conflict of Interest

The authors declare no conflict of interest.

## Keywords

backbone modulation, near-infrared, nonfullerene acceptors, organic solar cells

Received: March 27, 2019

Revised: May 21, 2019

Published online: June 12, 2019

- [1] Y. Lin, Y. Li, X. Zhan, *Chem. Soc. Rev.* **2012**, *41*, 4245.
- [2] C. B. Nielsen, S. Holliday, H. Y. Chen, S. J. Cryer, I. McCulloch, *Acc. Chem. Res.* **2015**, *48*, 2803.
- [3] G. Zhang, J. Zhao, P. C. Y. Chow, K. Jiang, J. Zhang, Z. Zhu, J. Zhang, F. Huang, H. Yan, *Chem. Rev.* **2018**, *118*, 3447.
- [4] Q. An, X. Ma, J. Gao, F. Zhang, *Sci. Bull.* **2019**, *64*, 504.
- [5] Y. Cui, H. Yao, L. Hong, T. Zhang, Y. Xu, K. Xian, B. Gao, J. Qin, J. Zhang, Z. Wei, J. Hou, *Adv. Mater.* **2019**, *31*, 1808356.
- [6] B. Fan, D. Zhang, M. Li, W. Zhong, Z. Zeng, L. Ying, F. Huang, Y. Cao, *Sci. China: Chem.* **2019**, *1*.
- [7] J. Yuan, Y. Zhang, L. Zhou, G. Zhang, H.-L. Yip, T.-K. Lau, X. Lu, C. Zhu, H. Peng, P. A. Johnson, M. Leclerc, Y. Cao, J. Ulanski, Y. Li, Y. Zou, *Joule* **2019**, *3*, 1140.
- [8] L. Meng, Y. Zhang, X. Wan, C. Li, X. Zhang, Y. Wang, X. Ke, Z. Xiao, L. Ding, R. Xia, H. L. Yip, Y. Cao, Y. Chen, *Science* **2018**, *361*, 1094.
- [9] B. Kan, H. Feng, X. Wan, F. Liu, X. Ke, Y. Wang, Y. Wang, H. Zhang, C. Li, J. Hou, Y. Chen, *J. Am. Chem. Soc.* **2017**, *139*, 4929.
- [10] Z. Zhang, J. Yu, X. Yin, Z. Hu, Y. Jiang, J. Sun, J. Zhou, F. Zhang, T. P. Russell, F. Liu, W. Tang, *Adv. Funct. Mater.* **2018**, *28*, 1705095.
- [11] W. Zhao, S. Zhang, Y. Zhang, S. Li, X. Liu, C. He, Z. Zheng, J. Hou, *Adv. Mater.* **2018**, *30*, 1704837.
- [12] Y. Yang, Z. G. Zhang, H. Bin, S. Chen, L. Gao, L. Xue, C. Yang, Y. Li, *J. Am. Chem. Soc.* **2016**, *138*, 15011.
- [13] Y. Lin, J. Wang, Z. G. Zhang, H. Bai, Y. Li, D. Zhu, X. Zhan, *Adv. Mater.* **2015**, *27*, 1170.
- [14] D. He, F. Zhao, J. Xin, J. J. Rech, Z. Wei, W. Ma, W. You, B. Li, L. Jiang, Y. Li, C. Wang, *Adv. Energy Mater.* **2018**, *8*, 1802050.
- [15] H. Yao, Y. Cui, R. Yu, B. Gao, H. Zhang, J. Hou, *Angew. Chem., Int. Ed.* **2017**, *56*, 3045.
- [16] Y. Chen, T. Liu, H. Hu, T. Ma, J. Y. L. Lai, J. Zhang, H. Ade, H. Yan, *Adv. Energy Mater.* **2018**, *8*, 1801203.
- [17] H. Yao, Y. Chen, Y. Qin, R. Yu, Y. Cui, B. Yang, S. Li, K. Zhang, J. Hou, *Adv. Mater.* **2016**, *28*, 8283.
- [18] X. Shi, J. Chen, K. Gao, L. Zuo, Z. Yao, F. Liu, J. Tang, A. K. Y. Jen, *Adv. Energy Mater.* **2018**, *8*, 1702831.
- [19] J. Zhu, Z. Ke, Q. Zhang, J. Wang, S. Dai, Y. Wu, Y. Xu, Y. Lin, W. Ma, W. You, X. Zhan, *Adv. Mater.* **2018**, *30*, 1704713.
- [20] J. Wang, J. Zhang, Y. Xiao, T. Xiao, R. Zhu, C. Yan, Y. Fu, G. Lu, X. Lu, S. R. Marder, X. Zhan, *J. Am. Chem. Soc.* **2018**, *140*, 9140.
- [21] B. Kan, J. Zhang, F. Liu, X. Wan, C. Li, X. Ke, Y. Wang, H. Feng, Y. Zhang, G. Long, R. H. Friend, A. A. Bakulin, Y. Chen, *Adv. Mater.* **2018**, *30*, 1704904.
- [22] Y. Li, J. D. Lin, X. Che, Y. Qu, F. Liu, L. S. Liao, S. R. Forrest, *J. Am. Chem. Soc.* **2017**, *139*, 17114.
- [23] X. Shi, X. Liao, K. Gao, L. Zuo, J. Chen, J. Zhao, F. Liu, Y. Chen, A. K. Y. Jen, *Adv. Funct. Mater.* **2018**, *28*, 1802324.
- [24] J. Wang, W. Wang, X. Wang, Y. Wu, Q. Zhang, C. Yan, W. Ma, W. You, X. Zhan, *Adv. Mater.* **2017**, *29*, 1702125.
- [25] H. Yao, L. Ye, J. Hou, B. Jang, G. Han, Y. Cui, G. M. Su, C. Wang, B. Gao, R. Yu, H. Zhang, Y. Yi, H. Y. Woo, H. Ade, J. Hou, *Adv. Mater.* **2017**, *29*, 1700254.
- [26] Y. Zhang, B. Kan, Y. Sun, Y. Wang, R. Xia, X. Ke, Y. Q. Yi, C. Li, H. L. Yip, X. Wan, Y. Cao, Y. Chen, *Adv. Mater.* **2018**, *30*, 1707508.
- [27] S.-L. Chang, F.-Y. Cao, W.-C. Huang, P.-K. Huang, K.-H. Huang, C.-S. Hsu, Y.-J. Cheng, *ACS Energy Lett.* **2018**, *3*, 1722.
- [28] Y. Wang, Y. Zhang, N. Qiu, H. Feng, H. Gao, B. Kan, Y. Ma, C. Li, X. Wan, Y. Chen, *Adv. Energy Mater.* **2018**, *8*, 1702870.
- [29] H.-H. Gao, Y. Sun, X. Wan, B. Kan, X. Ke, H. Zhang, C. Li, Y. Chen, *Sci. China Mater.* **2017**, *60*, 819.
- [30] Z. Xiao, X. Jia, D. Li, S. Wang, X. Geng, F. Liu, J. Chen, S. Yang, T. P. Russell, L. Ding, *Sci. Bull.* **2017**, *62*, 1494.
- [31] T. Li, S. Dai, Z. Ke, L. Yang, J. Wang, C. Yan, W. Ma, X. Zhan, *Adv. Mater.* **2018**, *30*, 1705969.
- [32] B. Kan, H. Feng, H. Yao, M. Chang, X. Wan, C. Li, J. Hou, Y. Chen, *Sci. China: Chem.* **2018**, *61*, 1307.
- [33] H. H. Gao, Y. Sun, X. Wan, X. Ke, H. Feng, B. Kan, Y. Wang, Y. Zhang, C. Li, Y. Chen, *Adv. Sci.* **2018**, *5*, 1800307.
- [34] D. Liu, L. Yang, Y. Wu, X. Wang, Y. Zeng, G. Han, H. Yao, S. Li, S. Zhang, Y. Zhang, Y. Yi, C. He, W. Ma, J. Hou, *Chem. Mater.* **2018**, *30*, 619.
- [35] D.-M. Smilgies, *J. Appl. Crystallogr.* **2009**, *42*, 1030.
- [36] J. Comyn, *Int. J. Adhes. Adhes.* **1992**, *12*, 145.
- [37] H. Feng, Y. Q. Yi, X. Ke, J. Yan, Y. Zhang, X. Wan, C. Li, N. Zheng, Z. Xie, Y. Chen, *Adv. Energy Mater.* **2019**, *9*, 1803541.
- [38] Y. Lin, Y. Jin, S. Dong, W. Zheng, J. Yang, A. Liu, F. Liu, Y. Jiang, T. P. Russell, F. Zhang, F. Huang, L. Hou, *Adv. Energy Mater.* **2018**, *8*, 1701942.
- [39] A. B. Svante Nilsson, A. Budkowski, E. Moons, *Macromolecules* **2007**, *40*, 8291.
- [40] Z. Zhou, S. Xu, J. Song, Y. Jin, Q. Yue, Y. Qian, F. Liu, F. Zhang, X. Zhu, *Nat. Energy* **2018**, *3*, 952.
- [41] K. Jiang, G. Zhang, G. Yang, J. Zhang, Z. Li, T. Ma, H. Hu, W. Ma, H. Ade, H. Yan, *Adv. Energy Mater.* **2018**, *8*, 1701370.
- [42] S. J. Xu, Z. Zhou, W. Liu, Z. Zhang, F. Liu, H. Yan, X. Zhu, *Adv. Mater.* **2017**, *29*.
- [43] X. Che, Y. Li, Y. Qu, S. R. Forrest, *Nat. Energy* **2018**, *3*, 422.
- [44] L. Zuo, X. Shi, S. B. Jo, Y. Liu, F. Lin, A. K. Jen, *Adv. Mater.* **2018**, *30*, 1706816.
- [45] Y. Cui, H. Yao, B. Gao, Y. Qin, S. Zhang, B. Yang, C. He, B. Xu, J. Hou, *J. Am. Chem. Soc.* **2017**, *139*, 7302.
- [46] M. Li, K. Gao, X. Wan, Q. Zhang, B. Kan, R. Xia, F. Liu, X. Yang, H. Feng, W. Ni, Y. Wang, J. Peng, H. Zhang, Z. Liang, H.-L. Yip, X. Peng, Y. Cao, Y. Chen, *Nat. Photonics* **2017**, *11*, 85.
- [47] F. Huang, *Acta Polym. Sin.* **2018**, *9*, 1141.